

W2S: A Joint Denoising and Super-Resolution Dataset

Ruofan Zhou*, Majed El Helou*, Daniel Sage, Thierry Laroche, Arne Seitz, Sabine Süsstrunk

École Polytechnique Fédérale de Lausanne (EPFL), Switzerland
 {ruofan.zhou,majed.elhelou}@epfl.ch

Abstract. Denoising and super-resolution (SR) are fundamental tasks in imaging. These two restoration tasks are well covered in the literature, however, only separately. Given a noisy low-resolution (LR) input image, it is yet unclear what the best approach would be in order to obtain a noise-free high-resolution (HR) image. In order to study joint denoising and super-resolution (JDSR), a dataset containing pairs of noisy LR images and the corresponding HR images is fundamental. We propose such a novel JDSR dataset, **Widefield2SIM** (W2S), acquired using microscopy equipment and techniques. W2S is comprised of 144,000 real fluorescence microscopy images, used to form a total of 360 sets of images. A set is comprised of noisy LR images with different noise levels, a noise-free LR image, and a corresponding high-quality HR image. W2S allows us to benchmark the combinations of 6 denoising methods and 6 SR methods. We show that state-of-the-art SR networks perform very poorly on noisy inputs, with a loss reaching $14dB$ relative to noise-free inputs. Our evaluation also shows that applying the best denoiser in terms of reconstruction error followed by the best SR method does not yield the best result. The best denoising PSNR can, for instance, come at the expense of a loss in high frequencies, which is detrimental for SR methods. We lastly demonstrate that a light-weight SR network with a novel texture loss, trained specifically for JDSR, outperforms any combination of state-of-the-art deep denoising and SR networks¹.

Keywords: Real Image Restoration Dataset, Denoising, Super-resolution, Microscopy Imaging, Joint Optimization

1 Introduction

Obtaining noise-free and high-resolution (HR) images are two fundamental objectives in image restoration and many imaging pipelines. Deep learning-based methods in denoising [2,40,47] and SR [44,52,53], are outperforming classic signal processing approaches. A major limitation in the literature is, however, the fact that these two restoration tasks are addressed separately. This is in great

* The first two authors have similar contributions.

¹ Code and data available at <https://github.com/widefield2sim/w2s>

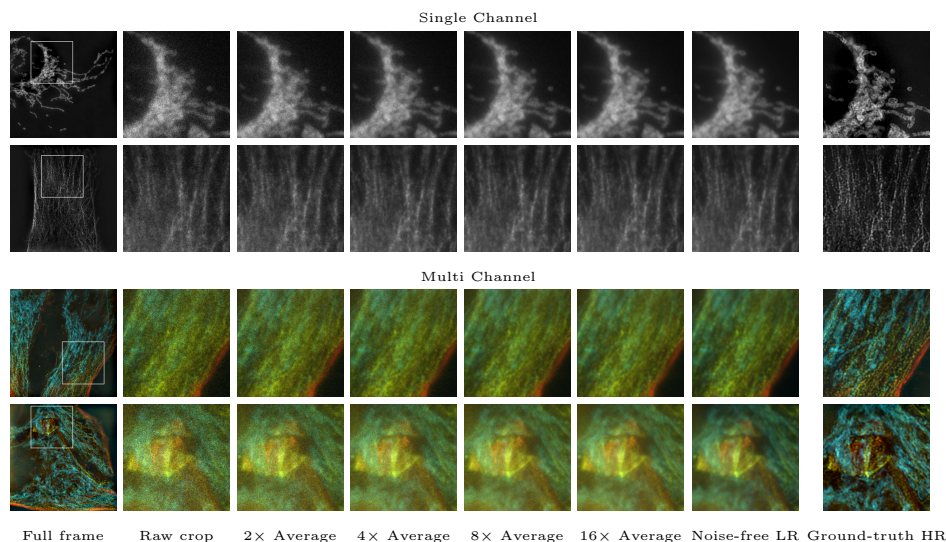


Fig. 1. Example of image sets in the proposed W2S. We obtain 5 LR images with different noise levels by taking a single raw image or averaging different numbers of raw images (of the same field of view). The more images we average (e.g., 2, 4, 8, and 16), the lower the noise level as shown in the figure. The noise-free LR images are the average of 400 raw images, and the HR images are obtained using structured-illumination microscopy (SIM) [17]. The multi-channel images are formed by mapping the three single-channel images of different wavelengths to RGB. A gamma correction is applied for better visualization. Best viewed on screen.

part due to a missing dataset that allows to train and evaluate joint denoising and super-resolution (JDSR). In this paper, we provide such a dataset.

To denoise and super-resolve an input image we can either (a) pass it through a denoiser and then an SR method, or (b) pass it directly through an SR method with the hope that it also removes the noise in the process. The first approach (a) is not desirable because two methods are needed instead of a single one, making the training slower and more importantly the inference slower at test time. The approach (b) is also not a reasonable solution, as state-of-the-art SR networks are sensitive to noise [9]. However, currently neither of these approaches can be evaluated, and new methods cannot be designed, in the absence of a proper JDSR dataset. Such a dataset must contain aligned pairs of LR and HR images, with noise and noise-free LR images, to be able to retrain prior denoising and SR methods on that dataset for benchmarking the consecutive application of a denoiser and an SR network.

We collect such a dataset, which, to the best of our knowledge, is the first JDSR dataset. We leverage microscopy equipment and techniques to acquire data satisfying the described requirements above. Our noisy LR images are captured using widefield imaging of human cells. We capture a total of 400 replicas raw

images per field of view, 8 times more than a recent denoising-only dataset using similar technology [51]. We average several of the LR images to obtain images with different noise levels, and all of the 400 replicas to obtain the noise-free LR image. We leverage the SIM technique [17] to obtain high-quality HR images. Using this acquisition setup, we create **Widefield2SIM** (W2S), which consists of 360 sets of LR and HR image pairs, with different fields of view, and acquisition wavelengths. Visual examples of the images in W2S are shown in Fig. 1.

We leverage our JDSR dataset to benchmark different approaches for solving denoising and SR restoration. We compare the sequential use of different denoisers and SR methods, of directly using an SR method on a noisy LR image, and of using SR methods on the noise-free LR images of our dataset for reference. We additionally evaluate the performance of retraining SR networks on our JDSR dataset. Results show a significant drop of 8 to 14dB in the performance of SR networks when the low-resolution (LR) input is noisy compared to it being noise-free. We also find that the costly consecutive application of denoising and SR is better. It is, however, not as performing in terms of PSNR and perceptual texture reconstruction as training a single model on the JDSR task, due to the accumulation of error. The best results are obtained with a light-weight model that we propose, trained with a novel texture loss that exploits the second-order statistics of feature maps.

In summary, we create the first real JDSR dataset, W2S, containing noisy images with 5 noise levels, noise-free LR images, and the corresponding high-quality HR images. We analyze our dataset by comparing the noise magnitude, the blur kernel, and the power spectral density (PSD) of our images, to those of existing denoising and SR datasets. We benchmark state-of-the-art denoising and SR algorithms on W2S, by evaluating different settings and on different noise levels. We train a single model for JDSR with a novel texture loss and show it achieves the best reconstruction error and perceptual results.

2 Related Work

2.1 Datasets for Denoising and Super-resolution

Several datasets have commonly been used for benchmarking SR and denoising, including Set5 [3], Set14 [46], BSD300 [28], Urban100 [19], Manga109 [29], and DIV2K [41]. Although these datasets contain various content ranging from nature photographs to comics images, they only allow for synthetic evaluation. Specifically, the noisy inputs are generated by adding Gaussian noise for testing denoising algorithms, and the LR images are generated by downsampling the blurred HR images for testing SR methods. These degradation models deviate from the degradations encountered in real image capture [7]. To better take into account realistic camera characteristics and thus evaluate denoising and SR methods in real scenarios, real-world denoising and SR datasets have recently been proposed. Here we discuss these real datasets and compare them to our proposed W2S.

Real Denoising Dataset Only a few studies quantitatively evaluate denoising algorithms on real images, such as DND [32], SSID [1]. These datasets capture images with different noise levels by changing the ISO setting at capture. More related to our work, zhang *et al.* [51] collect a dataset of microscopy images. All three datasets are designed only for denoising, and no HR images are provided that would allow them to be used for SR evaluation. According to our benchmark results, the best denoising algorithm does not necessarily provide the best input for the downstream SR task. This suggests a dataset on joint denoising and SR could provide a more comprehensive benchmark for image restoration.

Real Super-resolution Dataset Recently, the capture of LR and HR image pairs by changing the parameters of the capturing device has been proposed. Chen *et al.* collected 100 pairs of images of printed postcards placed at different distances. SR-RAW [50] consists of 500 real scenes captured with multiple focal lengths. Although this dataset provides real LR-HR pairs, it suffers from misalignment due to the inevitable perspective changes or lens distortion. Cai *et al.* thus introduce an image registration algorithm into the acquisition of another dataset, RealSR [5]. However, the problem of color mismatch still exists in that dataset. Moreover, to have high-quality images, all these datasets are captured with a low ISO setting, and the images thus contains very little noise as shown in our analysis. Qian *et al.* propose a dataset for joint demosaicing, denoising and SR [33], but the noise in their dataset is simulated by adding white Gaussian noise. Contrary to these datasets, our proposed W2S is constructed by using SR microscopy techniques [17], all pairs of images are well aligned, and it contains raw LR images with different noise levels and the noise-free LR images, thus enabling the benchmarking of both denoising and SR under real settings.

2.2 Deep Learning based Image Restoration

Deep learning-based methods have shown promising results on various image restoration tasks, including denoising and SR. We briefly present the previous work and the existing problems that motivate joint optimization.

Deep Learning for Denoising Recent deep learning approaches for image denoising achieve state-of-the-art results on recovering the noise-free images from images with additive noise such as Gaussian noise. They outperform classical methods like BM3D [10]. Whether based on residual learning [47], using memory blocks [40], or attention mechanisms [2], these deep learning methods all require training data. For real-world raw-image denoising, the training data should include noisy images with a Poisson noise component, and a corresponding aligned noise-free images, which is not easy to acquire. However, these networks are evaluated only on the denoising task, often only the one they are trained on. They optimize for minimal squared pixel error, leading to potentially smoothed out results that favour reconstruction error at the expense of detail preservation. When a subsequent task such as SR is then applied on the denoised outputs from these networks, the quality of the final results does not, as we see in our benchmark, necessarily correspond to the denoising performance of the different

approaches. This highlights the need for a more comprehensive perspective that jointly considers both restoration tasks.

Deep Learning for Super-resolution Since the first convolutional neural network for SR [12] outperformed conventional methods on synthetic datasets, many new architectures [21,25,38,42,44,52,53] and loss functions [20,23,36,49,54] have been proposed to improve the effectiveness and the efficiency of the networks. To improve the generalization of the SR networks on the real-world LR images where the degradation is unknown, kernel prediction [5,16] and kernel modeling [48,56] have been proposed. However, most of the SR networks assume that the LR images are noise-free or contain additive Gaussian noise with a very small variance. Their predictions are easily affected by the noise if the distribution of the noise is different from their assumptions [9]. This motivates us to jointly address the denoising and SR in this paper.

Joint Optimization in Deep Image Restoration Recent works have shown the power of joint optimization in image restoration. For example, the joint demosaicing and denoising [15,22], joint demosaicing and super-resolution [50,55], all these methods have shown that the joint solution outperforms the sequential application of the two stages. More relevant to JDSR, Xie *et al.* [45] present a dictionary learning approach with constraints tailored for depth maps, Chen *et al.* [8] propose a GAN-based model for JDSR, Miao *et al.* [30] propose a cascade of two networks for joint denoising and deblurring. All these methods are trained and tested on synthetic data and do not apply to real images. In our work, we propose the joint solution for JDSR on the real data to obtain optimal results.

3 Joint Denoising and Super-Resolution Dataset

To overcome the acquisition difficulties mentioned in Sec. 2.1, we turn to microscopy as it allows us to capture LR-HR pairs without alignment or color mismatch problems. In this section, we describe the experimental setup that we use to acquire the sets of LR and HR images and present an analysis of our dataset covering noise levels, blur kernels, and power spectral density comparisons.

3.1 Structured-Illumination Microscopy

Structured-illumination microscopy (SIM) is a technique used in microscopy imaging that allows samples to be captured with a higher resolution than the one imposed by the physical limits of the imaging system [17]. Its operation is based on the interference principle of the Moiré effect. We present how SIM works in more detail in our supplementary material. We use SIM to extend the resolution of standard widefield microscopy images. This allows us to obtain aligned LR and HR image pairs to create our dataset. The acquisition details are described in the next section.

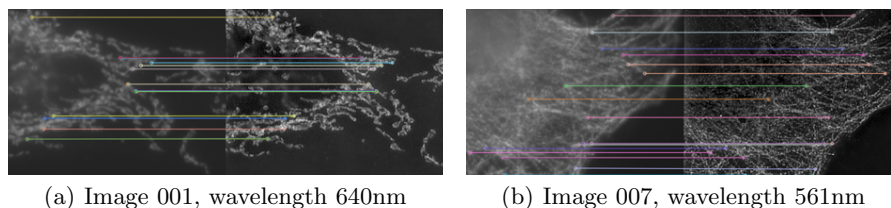


Fig. 2. Keypoint matching with a brute-force approach using Hamming distance, on the ORB detector and descriptor. In both figures, the left half is our ground-truth noise-free widefield image, and the right half is our SIM capture with a bicubic downsampling. A gamma correction is applied to the raw images for better visualization.

3.2 Data Acquisition

We capture the W2S dataset using widefield microscopy [43]. Images were acquired with a high-quality commercial fluorescence microscope and with real biological samples.

Widefield Images A time-lapse widefield of 400 images is acquired using a Nikon SIM setup (Eclipse T1) microscope. The details of the setup are given in the supplementary material. In total, we capture 120 different fields-of-view (FOVs), each FOV with 400 captures in 3 different wavelengths. All images are *raw*, i.e., are linear with respect to focal plane illuminance, and have a resolution of 512×512 pixels. We generate different noise-level images by averaging 2, 4, 8, and 16 raw images of the same FOV. The larger the number of averaged raw images is, the lower the noise level. The noise-free LR image is estimated as the average of all 400 captures of a single FOV. Examples of images with different noise levels and the noise-free LR image are presented in Fig. 1.

SIM Imaging The HR images are captured using SIM. We acquire the SIM images using the same Nikon SIM setup (Eclipse T1) microscope as above. We present the details of the setup in the supplementary material. The HR images’ resolution is higher by a factor of 2, resulting in a resolution of 1024×1024 .

Alignment As the acquisition process of LR and HR images is controlled through software that runs the microscope, and the device is well-stabilised throughout the capturing process, all images captured for a single FOV are very well aligned. However, we in addition verified the alignment of the images in post-processing. We use brute force matching based on the Hamming distance, with ORB [35] (FAST keypoint detector [34] and BRIEF descriptor [6]). The matching is carried out between our LR and HR pairs, after a bicubic downsampling of the HR images. We show two keypoint alignment examples in Fig. 2. After discarding incorrectly-matched keypoints, we find that the estimated keypoint translation between image pairs is zero and the homography is equal to the identity matrix. We use this registration approach to validate that all image pairs are indeed well-aligned, and no human error occurred during the acquisition steps.

3.3 Data Analysis

W2S includes 120 different FOVs, each FOV is captured in 3 channels (corresponding to the wavelengths of 488nm, 561nm and 640nm). As the texture of the cells are different and independent in different channels [37], the different channels can be counted as different images, thus resulting in 360 views. For each view, 1 HR image and 400 LR images are captured. We obtain LR images with different noise levels by averaging different numbers of images of the same FOV and the same channel. In summary, W2S provides 360 different sets of images, each image set includes LR images with 5 different noise levels (corresponding to 1, 2, 4, 8, and 16 averaged LR images), the corresponding noise-free LR image (averaged over 400 LR images) and the corresponding HR image acquired with SIM. The LR images have a resolution of 512×512 , the HR images of 1024×1024 .

To quantitatively evaluate the difficulty of recovering the HR image from the noisy LR observation in W2S, we analyse the degradation model of how the LR observations are obtained from the HR image. We use a commonly used degradation model [7,12,16,56], with an additional noise component,

$$I_{LR}^{noisy} = (I_{HR} \otimes k) \downarrow_m + n, \quad (1)$$

where I_{LR}^{noisy} and I_{HR} correspond, respectively, to the noisy LR observation and the HR image, \otimes is the convolution operation, k is a blur kernel, \downarrow_m is a downsampling operation with a factor of m , and n is the additive noise. Note that n is usually assumed to be 0 in most of the SR networks’ imaging models, while it is not the case for our dataset. As the downsampling factor m is equal to the targeted super-resolution factor, it is well defined for each dataset. We thus analyse the two unknown variables of the degradation model for W2S; the noise n and the blur kernel k .

Noise Estimation We use the noise modeling method in [14] to estimate the noise magnitude in raw images from W2S, from the denoising dataset FMD [51], and from the SR datasets RealSR [5] and City100 [7]. The approach of [14] models the noise as Poisson-Gaussian, where the measured noisy pixel intensity is given by $y = x + n_P(x) + n_G$. x is the noise-free pixel intensity, n_G is zero-mean Gaussian noise, and $x + n_P(x)$ follows a Poisson distribution. This approach yields an estimate for the parameter of the Poisson distribution. We evaluate the Poisson parameter of the noisy images from the three noise levels (obtained by averaging 1, 4 and 16 images) of W2S, the raw noisy images of FMD, and the LR images of the SR datasets for comparison. We show the mean of the estimated noise magnitude for the different datasets in Fig. 3(a). We see that the raw noisy images of W2S have a high noise level, comparable to that of FMD. On the other hand, the estimated noise parameters of the SR datasets are almost zero, up to small imprecision, and are thus significantly lower than even the estimated noise magnitude of the LR images from the lowest noise level in W2S. Our evaluations demonstrates that additive noise, such as Poisson noise, is not taken into consideration in current state-of-the-art SR datasets. The learning-based SR methods using these datasets are consequently not tailored to deal

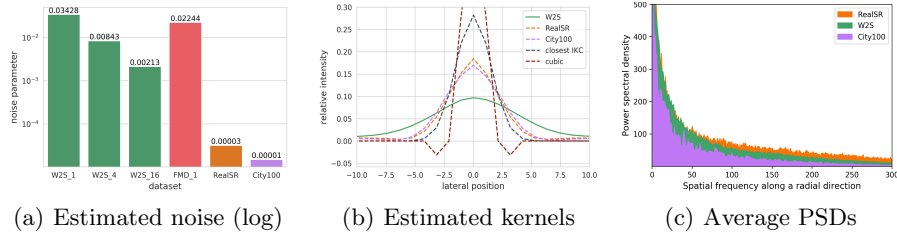


Fig. 3. Noise and kernel estimation and average PSDs of different datasets. A higher noise and a wide kernel indicate that the HR images of W2S are challenging to recover from the noisy LR. The PSD plots show that although W2S is comprised of microscopy images, these images have a similar spatial frequency distribution as the natural image datasets RealSR and City100.

with noisy inputs that are common in many practical applications, leading to potentially poor performance. In contrast, W2S contains images with high (and low) noise magnitude comparable to the noise magnitude of a state-of-the-art denoising dataset [51].

We compare W2S with other denoising datasets, DND [9], SSID [1], FMD [51] and other SR datasets, SR-RAW [50], City100 [7], RealSR [5]. The summary of the characteristics of the datasets is in Table 1. W2S contains 400 noisy images for each view, DND contains only 1, SSID contains 150, and FMD, which also uses widefield imaging contains 50. W2S can thus provide a wide range of noise levels by averaging a varying number of images out of the 400. In addition, W2S provides LR and HR images that do not suffer from alignment problems and color mismatch.

Blur Kernel Estimation We estimate the blur kernel k shown in Eq. (1) as

$$k = \underset{k}{\operatorname{argmin}} \|I_{LR}^{\text{noise-free}} \uparrow^{\text{bic}} - k \otimes I_{HR}\|_2^2, \quad (2)$$

where $I_{LR}^{\text{noise-free}} \uparrow^{\text{bic}}$ is the noise-free LR image upsampled using bicubic interpolation. We solve for k directly in the frequency domain using the Fast Fourier Transform to avoid the need for a lengthy optimization [13].

We use the aforementioned method to estimate the blur kernel k of W2S on the HR image and the noise-free LR image. The estimated blur kernel is visualized in Fig. 3(b). For the purpose of comparison, we show the estimated blur kernel from two SR datasets: RealSR [5] and City100 [7]. We also visualize the two other blur kernels: the MATLAB bicubic kernel that is commonly used in the synthetic SR datasets, and the Gaussian blur kernel with a sigma of 2.0 which is the largest kernel used by the state-of-the-art blind SR network [16] for the upscaling factor of 2. From the visualization we clearly see the bicubic kernel and Gaussian blur kernel that are commonly used in synthetic datasets are much different from the blur kernels of real captures. The blur kernel of W2S has a long tail compared to the blur kernels estimated from the other SR

	Dataset	RAW		Alignment	Color matching	# Noisy LR images	Main type of noise	# Ground-truth images
		LR	HR					
Denoising	DND [32]	✓	✗	Yes	Yes	1	Gaussian	50
	SSID [1]	✓	✗	Yes	Yes	150	Gaussian	200
	FMD [51]	✓	✗	Yes	Yes	50	Poisson	240
SR	SR-RAW [50]	✓	✗	No	No	0	None	500
	City100 [7]	✗	✗	Yes	Yes	0	None	100
	RealSR [5]	✗	✗	Yes	No	0	None	598
	W2S	✓	✓	Yes	Yes	400	Poisson	360

Table 1. Characteristics of different state-of-the-art denoising and SR datasets. Our W2S contains noisy LR images, a noise-free LR image, and the corresponding HR image, thus enabling joint denoising and super-resolution (JDSR) evaluations.

datasets, illustrating that more high-frequency information is removed for the LR images in W2S, and thus making the recovery of HR images from these LR images much more challenging.

Compared to the SR datasets, the LR and HR pairs in W2S are well-aligned during the capture process, and no further registration is needed. On the other hand, to obtain high-quality images, the SR datasets are captured under high ISO and contain almost zero noise. W2S contains LR images with different noise levels, which makes it a more comprehensive benchmark for testing under different imaging conditions. Moreover, as shown in Sec. 3.3, the estimated blur kernel of W2S is wider than that of other datasets, and hence averages pixels over a larger window, making W2S a more challenging dataset for SR.

Power Spectral Density To illustrate that the images of W2S share similar spatial frequency characteristics as other datasets, we plot the average power spectral density (PSD) for W2S and two other SR datasets City100 [7] and RealSR [5], which contain natural images, in Fig. 3(c). The PSD curve of W2S lies between the PSD curves of City100 [7] and RealSR [5], and shares a similar distribution that follows the well-known $1/f$ natural image power-law as a function of spatial frequency [4].

4 Benchmark

We benchmark on the sequential application of state-of-the-art denoising and SR algorithms on W2S. Note that we do not consider the inverse order, i.e., applying SR on noisy images, as this will amplify the noise and cause a large decrease in PSNR as shown in the last row of Table 3. With current methods, it would be impossible for a subsequent denoiser to recover the real signals.

4.1 Setup

We split W2S into two disjoint training and test sets. The training set consists of 240 sets of LR and HR images, and the test set consists of 120 sets of images. There is no overlap between the training set and the test set. We retrain the learning-based methods on the training set. The evaluation of all methods is on the test set.

Method	Number of raw images averaged before denoising				
	1	2	4	8	16
PURE-LET [26]	37.29/0.939	38.93/0.952	40.83/0.964	42.44/0.972	44.05/0.977
VST+EPLL [57]	37.51/0.951	39.56/0.965	41.59/0.973	43.36/0.980	45.16/0.984
VST+BM3D [10]	37.80/0.955	39.78/0.967	41.78/0.975	43.52/0.980	45.30/0.985
DnCNN [†] [47]	38.20/0.952	39.40/0.963	41.54/0.972	43.16/0.977	44.13/0.978
MemNet [†] [40]	38.25/0.952	39.69/0.962	41.04/0.970	42.84/0.976	44.45/0.980
RIDNet [†] [2]	37.82/0.949	38.99/0.958	41.47/0.970	42.07/0.975	44.95/0.982

Table 2. PSNR (dB)/SSIM results on denoising the W2S test images. We benchmark a variety of standard methods, three classical ones (of which PURE-LET is designed for Poisson noise removal), and three deep learning based methods. The larger the number of averaged raw images is, the lower the noise level. [†]These learning-based methods are trained for each noise level separately, on our training set. A very interesting observation is that the best PSNR results (in red) do not necessarily give the best result after the downstream SR method, as we see in Table 3. We highlight the results under highest noise level with gray background for easier comparison with Table 3.

For denoising, we evaluate different approaches from both classical methods and deep-learning methods. We use a method tailored to address Poisson denoising, PURE-LET [26], and the classical Gaussian denoising methods EPLL [57] and BM3D [10]. The Gaussian denoisers are combined with the Anscombe variance-stabilization transform (VST) [27] to first modify the distribution of the image noise into a Gaussian distribution, denoise, and then invert the result back with the inverse VST. We estimate the noise magnitude using the method in [14], to be used as input for both the denoiser and for the VST when the latter is needed. We also use the state-of-the-art deep-learning methods DnCNN [47], MemNet [40], and RIDNet [2]. For a fair comparison with the traditional non-blind methods that are given a noise estimate, we train each of these denoising methods for every noise level separately, and test with the appropriate model per noise level. The training details are presented in the supplementary material.

We use six state-of-the-art SR networks for the benchmark: four pixel-wise distortion-based SR networks, RCAN [52], RDN [53], SAN [11], SRFBN [24], and two perceptually-optimized SR networks, EPSR [42] and ESRGAN [44]. The networks are trained for SR and the inputs are assumed to be noise-free, i.e., they are trained to map from the noise-free LR images to the high-quality HR images. All these networks are trained using the same settings, the details of which are presented in the supplementary material.

4.2 Results and Discussion

We apply the denoising algorithms on the noisy LR images, and calculate the PSNR and SSIM values between the denoised image and the corresponding noise-free LR image in the test set of W2S. The results of the 6 benchmarked denoising algorithms are shown in Table 2. Comparing to the previous results on DND and SSID image datasets, the algorithms achieve lower PSNR values on W2S [1,2,32],

		Super-resolution networks					
		RCAN	RDN	SAN	SRFBN	EPSR	ESRGAN
Denoisers	PURE-LET	22.01/0.65	22.85/0.66	22.80/0.66	22.64/0.67	22.57/0.60	23.12/0.67
	VST+EPLL	24.16/0.71	24.71/0.71	24.57/0.72	24.21/0.71	23.76/0.64	24.13/0.70
	VST+BM3D	24.44/0.71	24.72/0.72	24.45/0.70	24.35/0.71	23.81/0.63	24.28/0.71
	DnCNN [†]	24.34/0.71	24.66/0.71	24.29/0.70	24.29/0.70	23.82/0.62	24.66 /0.71
	MemNet [†]	24.45/0.71	24.71/0.71	24.35/0.70	24.51/0.70	23.83/0.63	24.66 /0.70
	RIDNet [†]	24.52 /0.71	24.76 /0.71	24.64 /0.71	24.62 /0.71	23.86 /0.62	24.41/0.70
Noise-free LR		26.83/0.78	26.81/0.78	26.82/0.78	26.81/0.78	24.63/0.65	26.02/0.76
Noisy LR		12.56/0.27	17.39/0.41	15.24/0.38	19.38/0.43	16.37/0.36	16.64/0.38

Table 3. PSNR (dB)/SSIM results on the sequential application of denoising and SR methods on the W2S test images with the highest noise level, which correspond to the first column of Table 2. For each SR method, we highlight the best PSNR value in red. [†]The learning-based denoising methods are retrained for each noise level; the SR networks are trained to map the noise-free LR images to the high-quality HR images. Results on other noise levels are presented in the supplementary material.

illustrating that W2S contains more challenging noisy images. Denoisers based on deep learning outperform the classical denoising methods for the highest noise level (e.g., 1), however, BM3D achieves higher PSNR and SSIM when the noise level decreases (e.g. 2, 4, 8, 16). The molecular structure of the cells contain sufficient texture repetition for the block matching of BM3D to perform well, and when the noise level is not very high, the generative power of deep-learning methods is not as solicited. However, one very interesting observation is that a higher PSNR results, in some cases, in unwanted smoothing in the form of a local filtering or averaging that incurs a loss of detail. Although the PSNR results of RIDNet are not the best (Table 2), when they are used downstream by the SR networks in Table 3, the RIDNet images achieve the best performance.

The SR networks are applied on the denoised results of the denoising algorithms mentioned above. We show the PSNR and SSIM results in Table 3 for the highest noise level (grey background column in 3). We also include the results of applying the SR networks on the noise-free LR images. We see that although the four distortion-based SR networks (RCAN, RDN, SAN, SRFBN) have very similar performance when applied on the noise-free LR images (the largest difference in PSNR is 0.02dB, between RCAN and SRFBN), we see larger difference when these networks are applied to the denoised images of the previous step. We notice that there is a significant drop in PSNR and SSIM when the SR networks receive the denoised LR images instead of the noise-free LR images, even though the difference between the denoised LR images and the noise-free LR images are small. For example, applying RDN on noise-free LR images results in a PSNR value of 26.81dB, while the PSNR value of the same network applied to the denoised results of RIDNet on the lowest noise level is 25.85dB (shown in the first row, last column in Table 4). This illustrates the SR networks are strongly affected by noise in the inputs. Among all the distortion-based SR networks, RDN shows the most robustness as it outperforms all other networks in terms of PSNR when applied on denoised LR images. As mentioned above, another in-

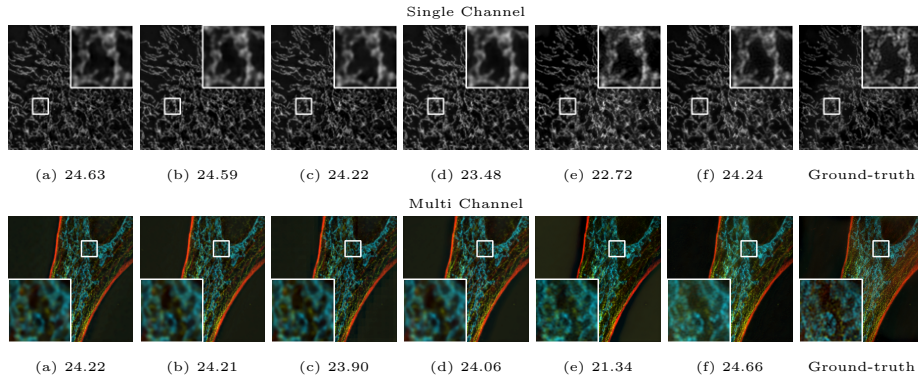


Fig. 4. Qualitative results with PSNR (dB) value on the sequential application of denoising and SR algorithms on the W2S test images with the highest noise level. (a) RIDNet [2]+RCAN [52], (b) RIDNet [2]+RDN [53], (c) RIDNet [2]+SAN [11], (d) RIDNet [2]+SRFBN [24], (e) RIDNet [2]+EPSR [42], (f) DnCNN [47]+ESRGAN [44]. The multi-channel images are formed by mapping the three single-channel images of different wavelengths to RGB. A gamma correction is applied for better visualization. Best viewed on screen.

interesting observation is that although RIDNet results in lower PSNR than other networks for denoising at the highest noise level, RIDNet still provides a better input for the SR networks.

Qualitative results are given in Fig. 4, where for each SR network we show the results for the denoising algorithm that achieves the highest PSNR value for the joint task. Notice that none of networks is able to produce results with detailed texture. As the denoising algorithms have removed some high-frequency signals as noise, the SR results from the distortion-based networks are blurry and many texture details are missing. Although the perception-based methods (EPSR and ESRGAN) are able to produce sharp results, they fail to reproduce faithful texture.

5 Joint Denoising and Super-Resolution (JDSR)

Our benchmark results in Sec. 4 show that the successive application of denoising and SR algorithms does not produce the highest-quality HR outputs. In this section, we demonstrate that it is more effective to train a JDSR model that directly transforms the noisy LR image into an HR image.

5.1 Texture Loss

To enable the network to better recover texture, we replace the GAN loss in the training with a novel texture loss. GAN loss usually results in SR networks producing realistic but fake textures that are different from the ground-truth and

Method	Number of raw images averaged before JDSR				#Parameters
	1	2	4	8	
RIDNet [†] +RDN [‡]	24.76/0.712	24.98/0.714	25.29/0.736	25.63/0.741	1.5M+22M
DnCNN [†] +ESRGAN [‡]	24.66/0.705	24.95/0.716	25.23/0.726	25.46/0.733	0.5M+16M
JDSR-RDN*	25.07/0.707	25.16/0.717	25.57/0.732	25.95/0.752	22M
JDSR-ESRGAN*	24.69/0.707	24.96/0.715	25.27/0.724	25.51/0.735	16M
Ours*	25.17/0.713	25.28/0.721	25.61/0.737	25.89/0.759	11M

Table 4. JDSR PSNR (*dB*)/SSIM results on the W2S test set. [†]The denoising networks are separately retrained per noise level. [‡]The SR networks are trained to map noise-free LR images to HR images. *The networks trained for JDSR are also retrained per noise level. For each noise level, we show the best PSNR and SSIM value in red.

may result in a significant drop in PSNR [44]. Instead, we introduce a texture loss that exploits the features’ second-order statistics to help the network to produce high-quality and real textures. This choice is motivated by the fact that traditional second-order descriptors have proven particularly effective for tasks such as texture recognition [18]. We leverage the second-order statistics of VGG features of the images to match the similarity of the texture. Our texture loss is defined as

$$\mathcal{L}_{texture} = \|Cov(\phi(I_{SR})) - Cov(\phi(I_{HR}))\|_2^2, \quad (3)$$

where I_{est} is the estimated result from the network for JDSR and I_{HR} is the ground-truth HR image, $\phi(\cdot)$ is a neural feature space, and $Cov(\cdot)$ computes the covariance. We follow the implementation of MPN-CONV [31] for the forward and backward feature covariance calculation.

5.2 Training Setup

For JDSR, we adopt a 16-layer RRDB architecture [44] followed by one pixel-shuffle up-convolution layer [38]. In order to improve the visual quality of the resulting image, we also incorporate perceptual loss into the training objective

$$\mathcal{L}_{perceptual} = \|\phi(I_{est}) - \phi(I_{HR})\|_2^2. \quad (4)$$

Our final loss function is

$$\mathcal{L} = \mathcal{L}_1 + \alpha \cdot \mathcal{L}_{perceptual} + \beta \cdot \mathcal{L}_{texture}, \quad (5)$$

where \mathcal{L}_1 represents the ℓ_1 loss between the estimated image and the ground-truth. We empirically set $\alpha = 0.05$ and $\beta = 0.05$. For the neural feature space, we use a pre-trained 19-layer VGG [39]. For the perceptual loss, we take the features from ‘conv1_2’, ‘conv2_2’, ‘conv3_4’, ‘conv4_4’ and ‘conv5_4’. For the texture loss, we take the features from ‘conv4_4’.

We follow the same training setup as the experiments in Sec. 4. For comparison, we also train RDN [53] and ESRGAN [44] on JDSR.

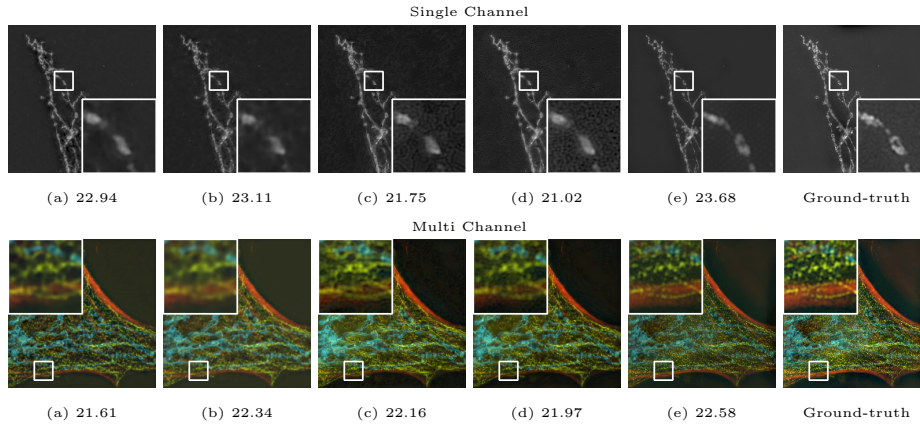


Fig. 5. Qualitative results (with the corresponding PSNR values) of denoising and SR on the W2S test images with the highest noise level. (a) RIDNet [2]+RDN [53], (b) RDN, (c) DnCNN [47]+ESRGAN [44], (d) ESRGAN, (e) a 16-layer RRDB [44] trained with our proposed texture loss. The results on the W2S test images with other noise levels are presented in our supplementary material. The multi-channel images are formed by mapping the three single-channel images of different wavelengths to RGB. A gamma correction is applied for better visualization. Best viewed on screen.

5.3 Results and Discussion

The quantitative results of different methods on different noise levels are reported in Table 4. The results indicate that comparing to the sequential application of denoising and SR, a single network trained on JDSR is more effective even though it contains less parameters. GAN-based methods generate fake textures and lead to low PSNR and SSIM scores. Our model, trained with texture loss, is able to outperform RDN and effectively recover high-fidelity texture information even when high noise levels are present in the LR inputs. We show the qualitative results of JDSR on the highest noise level (which corresponds to the first column of Table 2) in Fig. 5. We see that other networks have difficulties to recover the shape of the cells in the presence of noise, and that our method trained with texture loss is able to generate a higher-quality HR image with faithful texture.

6 Conclusion

We propose the first joint denoising and SR (JDSR) dataset: **Widefield2SIM**. We use image averaging to obtain LR images with different noise levels and the noise-free LR. The HR images are obtained through the SIM technique. With W2S, we benchmark the combination of various denoising and SR methods. Our results show that SR networks are very sensitive to noise, and that the consecutive application of two approaches is sub-optimal and suffers from the accumulation of errors from both stages. Our results also show the networks benefit from joint

optimization for denoising and SR. We train a single network for JDSR, with a novel texture loss to enable the network to reproduce faithful texture. W2S will be publicly available as a benchmark for joint denoising and SR, which we believe will be useful in advancing image restoration in real applications.

References

1. Abdelhamed, A., Lin, S., Brown, M.S.: A high-quality denoising dataset for smartphone cameras. In: CVPR (2018) [4](#), [8](#), [9](#), [10](#)
2. Anwar, S., Barnes, N.: Real image denoising with feature attention. ICCV (2019) [1](#), [4](#), [10](#), [12](#), [14](#)
3. Bevilacqua, M., Roumy, A., Guillemot, C., Alberi-Morel, M.L.: Low-complexity single-image super-resolution based on nonnegative neighbor embedding (2012) [3](#)
4. Burton, G.J., Moorhead, I.R.: Color and spatial structure in natural scenes. Applied optics (1987) [9](#)
5. Cai, J., Zeng, H., Yong, H., Cao, Z., Zhang, L.: Toward real-world single image super-resolution: A new benchmark and a new model. In: CVPR (2019) [4](#), [5](#), [7](#), [8](#), [9](#)
6. Calonder, M., Lepetit, V., Strecha, C., Fua, P.: Brief: Binary robust independent elementary features. In: ECCV. pp. 778–792 (2010) [6](#)
7. Chen, C., Xiong, Z., Tian, X., Zha, Z.J., Wu, F.: Camera lens super-resolution. In: CVPR (2019) [3](#), [7](#), [8](#), [9](#)
8. Chen, L., Dan, W., Cao, L., Wang, C., Li, J.: Joint denoising and super-resolution via generative adversarial training. In: ICPR (2018) [5](#)
9. Choi, J.H., Zhang, H., Kim, J.H., Hsieh, C.J., Lee, J.S.: Evaluating robustness of deep image super-resolution against adversarial attacks. In: ICCV (2019) [2](#), [5](#), [8](#)
10. Dabov, K., Foi, A., Katkovnik, V., Egiazarian, K.: Image denoising by sparse 3-D transform-domain collaborative filtering. TIP (2007) [4](#), [10](#)
11. Dai, T., Cai, J., Zhang, Y., Xia, S.T., Zhang, L.: Second-order attention network for single image super-resolution. In: CVPR (2019) [10](#), [12](#)
12. Dong, C., Loy, C.C., He, K., Tang, X.: Learning a deep convolutional network for image super-resolution. In: ECCV (2014) [5](#), [7](#)
13. El Helou, M., Dümbgen, F., Achanta, R., Süsstrunk, S.: Fourier-domain optimization for image processing. arXiv preprint (2018) [8](#)
14. Foi, A., Trimeche, M., Katkovnik, V., Egiazarian, K.: Practical Poissonian-Gaussian noise modeling and fitting for single-image raw-data. TIP (2008) [7](#), [10](#)
15. Gharbi, M., Chaurasia, G., Paris, S., Durand, F.: Deep joint demosaicking and denoising. TOG (2016) [5](#)
16. Gu, J., Lu, H., Zuo, W., Dong, C.: Blind super-resolution with iterative kernel correction. In: CVPR (2019) [5](#), [7](#), [8](#)
17. Gustafsson, M.G.: Surpassing the lateral resolution limit by a factor of two using structured illumination microscopy. Journal of microscopy (2000) [2](#), [3](#), [4](#), [5](#)
18. Harandi, M., Salzmann, M., Porikli, F.: Bregman divergences for infinite dimensional covariance matrices. In: CVPR (2014) [13](#)
19. Huang, J.B., Singh, A., Ahuja, N.: Single image super-resolution from transformed self-exemplars. In: CVPR (2015) [3](#)
20. Johnson, J., Alahi, A., Fei-Fei, L.: Perceptual losses for real-time style transfer and super-resolution. In: ECCV (2016) [5](#)

21. Kim, J., Kwon Lee, J., Mu Lee, K.: Accurate image super-resolution using very deep convolutional networks. In: CVPR (2016) [5](#)
22. Klatzer, T., Hammernik, K., Knobelreiter, P., Pock, T.: Learning joint demosaicing and denoising based on sequential energy minimization. In: ICCP (2016) [5](#)
23. Ledig, C., Theis, L., Huszár, F., Caballero, J., Cunningham, A., Acosta, A., Aitken, A., Tejani, A., Totz, J., Wang, Z., et al.: Photo-realistic single image super-resolution using a generative adversarial network. In: CVPR (2017) [5](#)
24. Li, Z., Yang, J., Liu, Z., Yang, X., Jeon, G., Wu, W.: Feedback network for image super-resolution. In: CVPR (2019) [10](#), [12](#)
25. Lim, B., Son, S., Kim, H., Nah, S., Mu Lee, K.: Enhanced deep residual networks for single image super-resolution. In: CVPR (2017) [5](#)
26. Luisier, F., Blu, T., Unser, M.: Image denoising in mixed Poisson-Gaussian noise. TIP (2011) [10](#)
27. Makitalo, M., Foi, A.: Optimal inversion of the generalized Anscombe transformation for Poisson-Gaussian noise. IEEE Transactions on Image Processing **22**(1), 91–103 (2012) [10](#)
28. Martin, D., Fowlkes, C., Tal, D., Malik, J.: A database of human segmented natural images and its application to evaluating segmentation algorithms and measuring ecological statistics. In: ICCV (2001) [3](#)
29. Matsui, Y., Ito, K., Aramaki, Y., Fujimoto, A., Ogawa, T., Yamasaki, T., Aizawa, K.: Sketch-based manga retrieval using manga109 dataset. Multimedia Tools and Applications (2017) [3](#)
30. Miao, S., Zhu, Y.: Handling noise in image deblurring via joint learning. arXiv preprint (2020) [5](#)
31. Peihua Li, Jiangtao Xie, Q.W., Zuo, W.: Is second-order information helpful for large-scale visual recognition? ICCV (2017) [13](#)
32. Plotz, T., Roth, S.: Benchmarking denoising algorithms with real photographs. In: CVPR (2017) [4](#), [9](#), [10](#)
33. Qian, G., Gu, J., Ren, J.S., Dong, C., Zhao, F., Lin, J.: Trinity of pixel enhancement: a joint solution for demosaicking, denoising and super-resolution. arXiv preprint (2019) [4](#)
34. Rosten, E., Drummond, T.: Machine learning for high-speed corner detection. In: ECCV. pp. 430–443 (2006) [6](#)
35. Rublee, E., Rabaud, V., Konolige, K., Bradski, G.: ORB: An efficient alternative to SIFT or SURF. In: ICCV. pp. 2564–2571 (2011) [6](#)
36. Sajjadi, M.S., Scholkopf, B., Hirsch, M.: EnhanceNet: Single image super-resolution through automated texture synthesis. In: ICCV (2017) [5](#)
37. Schneider, C.A., Rasband, W.S., Eliceiri, K.W.: NIH Image to ImageJ: 25 years of image analysis. Nature methods (2012) [7](#)
38. Shi, W., Caballero, J., Huszár, F., Totz, J., Aitken, A.P., Bishop, R., Rueckert, D., Wang, Z.: Real-time single image and video super-resolution using an efficient sub-pixel convolutional neural network. In: CVPR (2016) [5](#), [13](#)
39. Simonyan, K., Zisserman, A.: Very deep convolutional networks for large-scale image recognition. ICLR (2015) [13](#)
40. Tai, Y., Yang, J., Liu, X., Xu, C.: MemNet: A persistent memory network for image restoration. In: ICCV (2017) [1](#), [4](#), [10](#)
41. Timofte, R., Gu, S., Wu, J., Van Gool, L.: NTIRE 2018 challenge on single image super-resolution: Methods and results. In: CVPRW (2018) [3](#)
42. Vasu, S., Thekke Madam, N., Rajagopalan, A.: Analyzing perception-distortion tradeoff using enhanced perceptual super-resolution network. In: ECCVW (2018) [5](#), [10](#), [12](#)

43. Verveer, P.J., Gemkow, M.J., Jovin, T.M.: A comparison of image restoration approaches applied to three-dimensional confocal and wide-field fluorescence microscopy. *Journal of microscopy* (1999) [6](#)
44. Wang, X., Yu, K., Wu, S., Gu, J., Liu, Y., Dong, C., Qiao, Y., Change Loy, C.: ES-RGAN: Enhanced super-resolution generative adversarial networks. In: *ECCVW* (2018) [1](#), [5](#), [10](#), [12](#), [13](#), [14](#)
45. Xie, J., Feris, R.S., Yu, S.S., Sun, M.T.: Joint super resolution and denoising from a single depth image. *TMM* (2015) [5](#)
46. Zeyde, R., Elad, M., Protter, M.: On single image scale-up using sparse-representations. In: *International Conference on Curves and Surfaces* (2010) [3](#)
47. Zhang, K., Zuo, W., Chen, Y., Meng, D., Zhang, L.: Beyond a Gaussian denoiser: Residual learning of deep CNN for image denoising. *TIP* (2017) [1](#), [4](#), [10](#), [12](#), [14](#)
48. Zhang, K., Zuo, W., Zhang, L.: Deep plug-and-play super-resolution for arbitrary blur kernels. In: *CVPR* (2019) [5](#)
49. Zhang, W., Liu, Y., Dong, C., Qiao, Y.: RankSRGAN: Generative adversarial networks with ranker for image super-resolution. In: *ICCV* (2019) [5](#)
50. Zhang, X., Chen, Q., Ng, R., Koltun, V.: Zoom to learn, learn to zoom. In: *CVPR* (2019) [4](#), [5](#), [8](#), [9](#)
51. Zhang, Y., Zhu, Y., Nichols, E., Wang, Q., Zhang, S., Smith, C., Howard, S.: A Poisson-Gaussian denoising dataset with real fluorescence microscopy images. In: *CVPR* (2019) [3](#), [4](#), [7](#), [8](#), [9](#)
52. Zhang, Y., Li, K., Li, K., Wang, L., Zhong, B., Fu, Y.: Image super-resolution using very deep residual channel attention networks. In: *ECCV* (2018) [1](#), [5](#), [10](#), [12](#)
53. Zhang, Y., Tian, Y., Kong, Y., Zhong, B., Fu, Y.: Residual dense network for image super-resolution. In: *TPAMI* (2020) [1](#), [5](#), [10](#), [12](#), [13](#), [14](#)
54. Zhang, Z., Wang, Z., Lin, Z., Qi, H.: Image super-resolution by neural texture transfer. In: *CVPR* (2019) [5](#)
55. Zhou, R., Achanta, R., Ssstrunk, S.: Deep residual network for joint demosaicing and super-resolution. In: *Color and Imaging Conference* (2018) [5](#)
56. Zhou, R., Susstrunk, S.: Kernel modeling super-resolution on real low-resolution images. In: *ICCV* (2019) [5](#), [7](#)
57. Zoran, D., Weiss, Y.: From learning models of natural image patches to whole image restoration. In: *ICCV* (2011) [10](#)